Sustainable Energy & Fuels

ROYAL SOCIETY OF CHEMISTRY

PAPER

View Article Online
View Journal | View Issue

Cite this: *Sustainable Energy Fuels*, 2026, **10**, 1147

Asymmetric electrode configurations enhance operating power density and energy efficiency of an aqueous, electrode-decoupled titanium–cerium redox flow battery

Jing Xie, [a] Shrihari Sankarasubramanian[bc] and Vijay Ramani *[a]

Redox flow batteries (RFBs), with decoupled scaling in energy and power, are an attractive solution for grid scale energy storage. Given the low margins and extreme price sensitivity of electricity supply, it is critically important for RFBs to reduce capital and operating costs. Improving the operating power density and energy efficiency of the RFB is a pathway towards lowered costs, but achieving simultaneous improvements in both parameters is hampered by the fact that they are typically inversely correlated. This study demonstrates a 50% improvement in operating power density of an aqueous, electrode-decoupled titanium–cerium RFB without loss of energy efficiency through electrode engineering driven by fundamental investigations of charge-transfer kinetics at the Ti and Ce electrodes. Exploiting the significant difference in reaction kinetics between the Ti and Ce actives, the interfacial area and surface functionalization (affecting electrode–electrolyte contact angles and kinetics of charge transfer) of the electrode were optimized to increase operating power while reducing overall cell resistance. This resulted in an increase in operating current density of a Ti–Ce RFB from 100 mA cm^{-2} to 150 mA cm^{-2}, sustaining ~70% energy efficiency over 80 h and 100 cycles. Notably, this study shows the key role played by the rate limiting electrode and the effect of electrode surface area in improving its performance. Overall, this study offers a template to significantly improve the overall performance of kinetically limited aqueous RFBs without catalysts or electrolyte reformulation.

Received 29th August 2025
Accepted 16th January 2026

DOI: 10.1039/d5se01171j

rsc.li/sustainable-energy

1. Introduction

The development of large-scale, robust, and cost-effective energy storage systems, such as rechargeable batteries, is a critical component of transitioning to sustainable but intermittent energy sources such as solar and wind.[1–4] Among them, redox flow batteries (RFBs) are a promising candidate because of their unique advantage: the energy capacity storage and output power density are decoupled, allowing for independent scale-up, and thus great design flexibility.[5–7] Among the different types of RFBs, all vanadium ones (VRFBs), introduced in the 1980s, have been extensively studied and commercialized.[8] The use of vanadium redox couples on both sides (enabled by the prevalence of multiple readily soluble oxidation states of V) mitigates active species crossover (a common failure mode and source of performance loss) and provides a unique operational advantage.[9] However, the scaling up of VRFBs is limited by the high cost of vanadium and relatively low standard potential (1.26 V *vs.* the standard hydrogen electrode (SHE)), making it difficult to meet cost targets for grid scale energy storage.[10] Thus, moving away from vanadium as the active species is a potential solution, but a key barrier to moving away from the VRFB is the fact that few other elements in the periodic table exhibit the vanadium ion's characteristic of being soluble at more than 2 oxidation states. Alternately, techno-economic analysis (TEA) has shown that increasing the operating voltage and operating current density (translating to the operating power density) is critically important for reducing capital costs.[11] The capital costs have been found to be a strongly non-linear function of both operating voltage and operating current density, with capital costs for 6 different flow battery chemistries falling by 70–90% when the operating current density is increased from 10 mA cm^{-2} to >100 mA cm^{-2}.[11,12] TEA indicated capital cost reductions of ~50% for RFBs with elemental actives (all-V or Zn–Br) when the operating voltage increased from 0.6 V to 1.2 V.[11] Thus, increasing RFB operating current density to >100 mA cm^{-2} and the operating voltage to >1 V is expected to dramatically reduce capital costs. The levelized cost of storage

[a]*Department of Energy, Environmental and Chemical Engineering, Washington University in St. Louis, St. Louis, MO, 63130, USA. E-mail: xiejing@wustl.edu; ramani@wustl.edu*

[b]*Department of Biomedical Engineering and Chemical Engineering, The University of Texas at San Antonio, San Antonio, TX, 78249, USA. E-mail: shrihari.sankarasubramanian@utsa.edu*

[c]*Department of Mechanical, Aerospace and Industrial Engineering, The University of Texas at San Antonio, San Antonio, TX, 78249, USA*

(LCOS) has been shown to be strongly coupled to the capital cost and is further affected by cycle duration (with some studies showing 4–10 hour cycles being the optimum).[13] But alternatives to VRFBs considered in the studies referenced above suffer from their own issues such as crossover of active species, toxicity (Br), phase change/plating–stripping reactions leading to dendrite formation (Zn, Pb, *etc.*) and unwanted side reactions (evolution of hydrogen or oxygen). The titanium–cerium RFB, a relatively new chemistry first reported in 2019 solves these chemistry problems and has been shown to meet all DOE cost targets.[14,15] In particular, the Ti–Ce RFB employs a selective anion exchange membrane (AEM) separator that significantly impedes the crossover of the redox active cations, making it an "electrode-decoupled" system. In this study, starting with an already inexpensive RFB chemistry (titanium–cerium (Ti–Ce)), we demonstrate RFB electrode engineering methods that can achieve significant improvements in operating power density by increasing current density with minimal associated increase in overpotential.[14,15]

The Ti–Ce RFB is a relatively new system that has been shown to both meet DOE cost targets and have the ability to be cycled diurnally.[14,15] The Ce redox couple has been examined as a possible active for RFBs due to two advantages: a high standard potential (1.61 V *vs.* SHE) and abundant geographical availability with relatively low cost.[16,17] The major challenge of deploying the Ce redox couple in RFBs is that Ce solubility is limited in sulfuric acid (H_2SO_4), a typical supporting electrolyte. In H_2SO_4, Ce solubility has been reported to be below 0.5 M and decreases as the concentration of H_2SO_4 increases.[18] As an alternative, methanesulfonic acid (MSA) has been shown to increase Ce solubility significantly with an inverse relationship between the solubilities of Ce(III) and Ce(IV) as a function of MSA concentration.[19] The Ce redox couple utilizing MSA as the supporting electrolyte has been used in multiple RFBs, including Zn–Ce,[20] Pb–Ce,[21] and V–Ce.[22] Ti and its alloys have been widely utilized in medical treatment,[23] aerospace,[24] and automobiles.[25] In RFBs, Ti has been decorated onto electrodes or membranes as a catalyst to promote the performance of VRFBs and as the redox active species in some RFB systems.[26–28] In fact, the abundance and production rate of Ti is about 50 and 100 times that of V, respectively, contributing to a market price that is 1/10th of V.[28] Moreover, a standard potential of 0.19 V *vs.* SHE makes the Ti redox couple a good candidate for RFBs as it is less prone to the hydrogen evolution reaction (HER) during the operation of RFBs. In recent years, Ti-based RFBs, such as Fe–Ti[29] and Mn–Ti[30] systems have been proposed and studied. We have combined the Ti and Ce redox couples to develop a fully dissolved (*i.e.*, no phase change or plating/stripping process) RFB that leverages the inherent advantages of both couples.

Starting with a cost effective RFB chemistry that consists of earth-abundant elemental actives, we focused on increasing the activity of the electrodes while decreasing their contribution to overall RFB cell resistance so as to achieve higher operating current density without increasing the overpotential. Given that the electroactive species in a RFB is typically dissolved in the electrolyte, the electron transfer process occurs on high surface area, porous electrodes that typically avoid using catalysts to keep down the cost. Carbon felt (CF) is amongst the most commonly utilized electrode materials in RFBs due to its high surface area, good stability in an acidic environment, and high conductivity.[31] Carbon paper (CP) has also been used as an electrode candidate but the combination of significantly lower porosity (compared to CF) and the associated increase in pressure drop has meant that most existing studies on CP focus on VRFBs, where the reduction in ohmic losses enabled by the thinner CP electrode offers a significant advantage.[32] Typically,

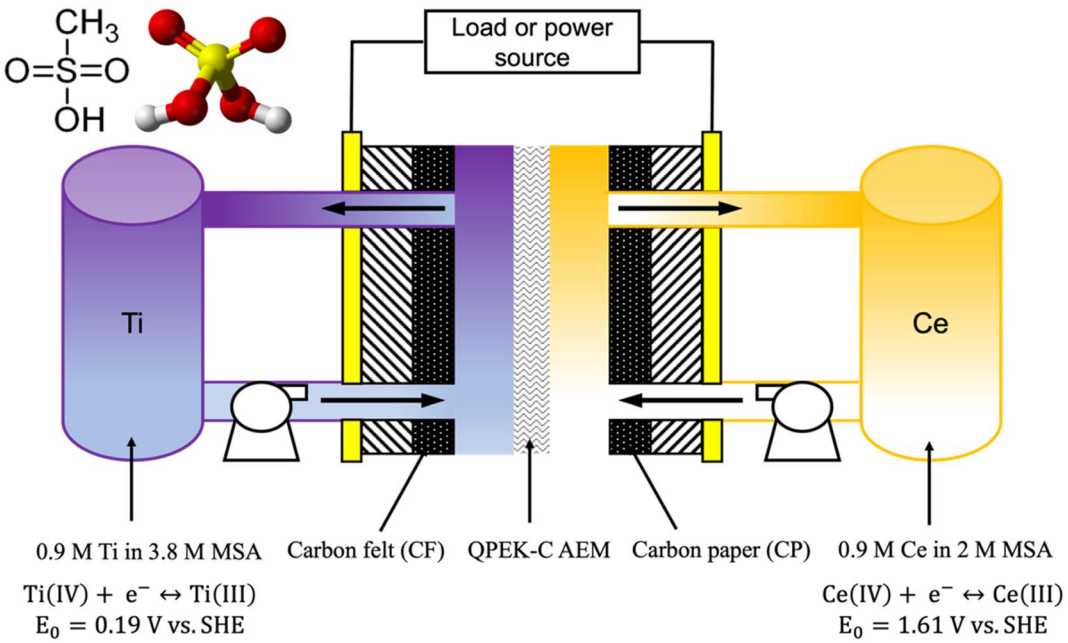

Scheme 1 Schematic illustration of a Ti–Ce RFB with an asymmetric electrode configuration. The separator is a custom anion exchange membrane (AEM), whose synthesis and characterization are detailed elsewhere.[70,71]

carbon electrodes are pretreated before RFB operation to enhance reactant transport and create surface functional groups that aid charge transfer kinetics, and heat treatment is a convenient method that has been extensively studied.[33,34] It has been recognized that significant performance improvements can be achieved by varying the electrode surface area, thickness and pre-treatment protocols. For example, Agar *et al.* and Li *et al.* investigated the performance-limiting side of VRFBs by applying CF with different pretreatment methods on the positive and negative sides and concluded that the performance of VRFBs was limited by the negative side.[35,36] Wei *et al.* showed that the electrochemical activity for the positive and negative sides of VRFBs was promoted by carbon nanofibers decorated with carbon nanotubes and Bi-based compounds, respectively.[37] Similarly, Jing *et al.* embedded tungsten and antimony on positive and negative carbon nanofibers, respectively, to achieve the highest performance of VRFBs.[38] Lu *et al.* provided evidence from a two-dimensional, transient model simulation that the performance of VRFBs could be further improved by applying a higher compression ratio of positive electrodes.[39] Nevertheless, the focus of a majority of these studies has been the impact on a particular RFB performance parameter, oftentimes to the detriment of other parameters. These studies improve the performance by (i) reducing ohmic losses by employing thinner electrodes or (ii) by decreasing activation polarization losses by electrode surface treatment and catalysts. It is challenging to employ both approaches in tandem as thinner electrodes have lower total surface area and thus reduce overall rate, while surface treatment of the electrodes or use of catalysts can reduce electrical conductivity and increase pressure drop, thereby increasing ohmic losses. Our study shows how fundamental studies of electrode kinetics and electrode wetting can be used to enable simultaneous decreases in activation polarization losses and ohmic polarization losses, and this was achieved in an electrode decoupled RFB where the two electrodes exhibit very different redox behaviors. Leveraging and extending the insights from these studies, we demonstrate a Ti–Ce RFB with an asymmetric electrode configuration successfully operated at 150 mA cm^{-2}, delivering an energy efficiency (EE) of 67.8% and capacity retention of 93% (Scheme 1). We present a roadmap for the use of fundamental electrochemical investigations (kinetics and transport studies using cyclic voltammetry) to downselect appropriate carbon electrodes for RFBs with the aim of maximizing cell level performance. The approach demonstrated with Ti–Ce RFBs can be equally applied to other systems.

2. Results and discussion

2.1 Effect of heat treatment on CP and CF

In order to confirm the potential modifications to both carbon electrodes brought by heat treatment, scanning electron microscopy (SEM) was used to examine the morphology of CP and CF before and after heat treatment, as presented in Fig. 1. CP was found to be composed of rigid and straight fibers, and no significant difference could be observed between pristine CP and heat-treated CP (HT CP). In contrast, CF was made of soft and curvy fibers, and the surface of CF fibers became rougher and more porous after heat treatment, indicating significant surface modification and potential increase in surface area. Energy dispersive X-ray (EDX) spectra showed that the oxygen content remained mostly unchanged between CP and HT CP, while a significant increase in surface oxygen was detected on CF post heat treatment (see Table 1). This correlation between surface morphology and surface oxygen content agrees with prior results showing that the thermal treatment oxidizes the carbon surface.[34] The results of surface investigations using X-ray photoelectron spectroscopy (XPS) are depicted in Fig. 2 (XPS survey spectra are depicted in Fig. S1). The C 1s data show minimal changes in case of CP while the percentage of C–C was found to decrease and the percentage of C=C increased in the case of CF, indicating an increase in C defect sites on the surface necessitating the formation of unsaturated C=C bonds. This was coupled with an increase in C–OH and C=O groups, indicating the presence of at least 3 different potential reaction sites on the surface. Oxygen functional groups were found to increase in percentage on HT CF, while there was not much difference between the XPS results of CP and HT CP. Interestingly, ether groups increased after thermal treatment, indicating that some of the C defect sites were being occupied by O. The ratio between alcohol groups and carbonyl groups inverted following thermal treatment, indicating oxidation of the alcohol groups to the corresponding carboxyl group. Given the difference in electrochemical activity between surface alcohol and carboxyl groups, the ratio between these groups would significantly affect the activity of a given carbon electrode, and this explains the impact of thermal treatment duration on carbon electrode activity. The change of CF by heat treatment was consistent with previous studies that applied CF as electrodes in VRFBs.[33,36,40] The percentages of various functional groups in different samples as measured by XPS are listed in Table 2. It was also proposed by these studies that the oxygen functional groups could work as catalytic sites to enhance the kinetics of vanadium redox reactions, and similar positive effects on Ti reactions were found in our study, which will be discussed further. The number of studies on the effects of heat treatment on CP is still limited, possibly because CP is not used as widely as CF. One previous study pointed out that the effect of thermal treatment on CP was nuanced and controlled by several factors (*e.g.*, microstructure and surface chemistry).[34]

2.2 Effect of thermal treatment on electrode–electrolyte interaction

During the operation of RFBs, electrolytes flow into the cell to contact the electrode, where the reactions take place, and high hydrophilicity is desirable to reduce mass transfer resistance.[32] The effect of electrode thermal treatment on the interfacial contact between the Ti and Ce electrolytes and the CF and CP electrodes was characterized through contact angle measurements using a goniometer. The contact angle was measured using ImageJ 1.54g (Java 1.8.0_345, 64-bit) from pictures captured from the goniometer. The side views of Ti and Ce electrolyte droplets on carbon electrodes are displayed in Fig. 3,

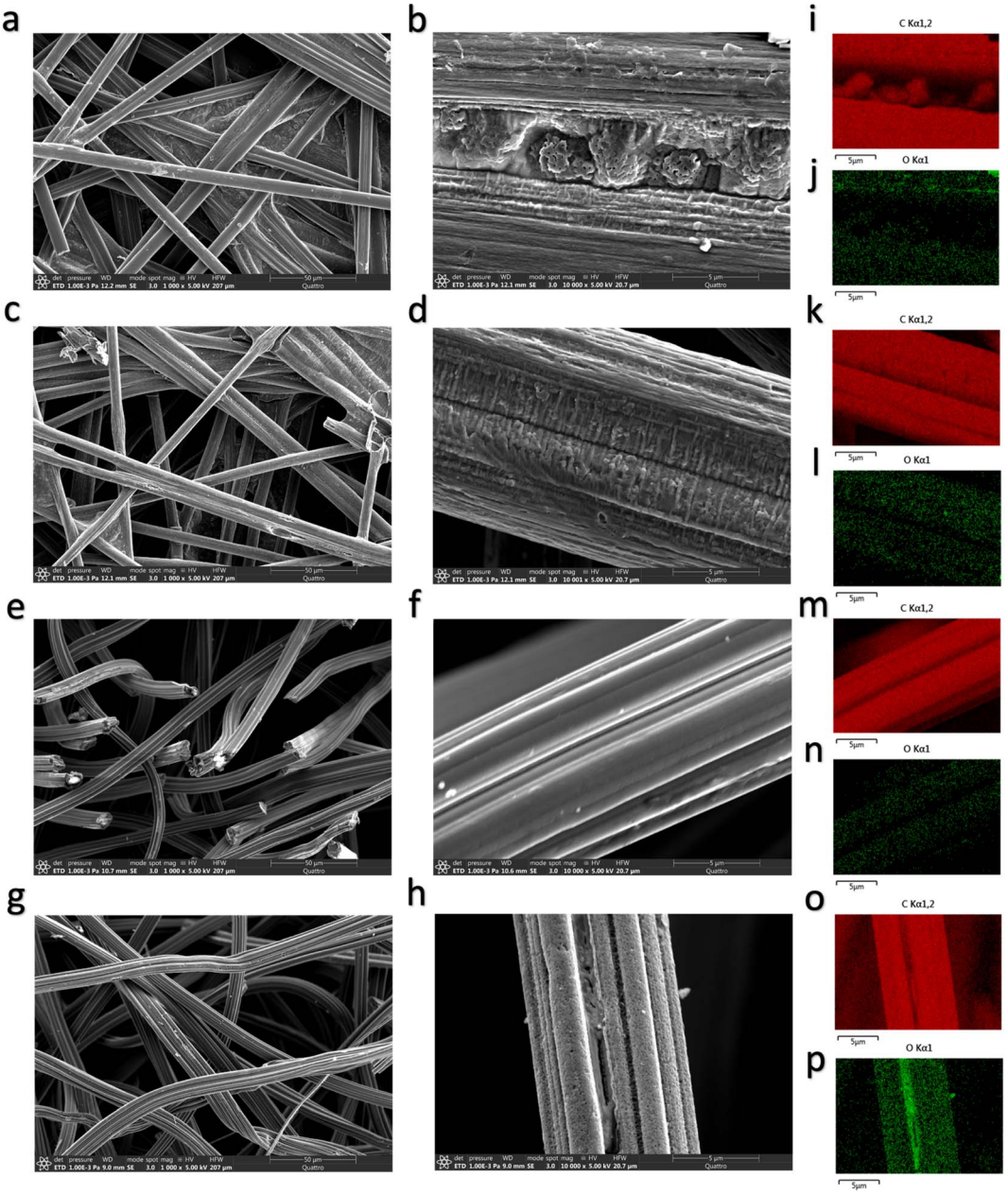

Fig. 1 SEM/EDX images of pristine CP (a, b, i and j), HT CP (c, d, k and l), pristine CF (e, f, m and n), and HT CF (g, h, o and p).

and the contact angle values are presented in Table 3. As shown in Fig. 3, both the Ti and Ce electrolytes readily spread and were absorbed into the porous electrode bulk in the case of CF and HT CF (no apparent bubble is seen visually). The Ce electrolyte also exhibited ready absorption and no apparent bubble formation in the case of CP and HT CP. However, the Ti electrolyte formed very obviously shaped droplets on CP, HT CP, and CF, indicating poor wettability. Thus, both the surface functional groups themselves and the characteristics of the electrolyte determine interfacial contact. The excellent hydrophilicity exhibited by HT CF with both Ce and Ti electrolytes was ascribed to the oxygen functional groups,[41] which was confirmed by SEM/EDX and XPS. Interestingly, all four types of electrodes exhibited good hydrophilicity with Ce electrolyte, indicating that the initial percentage of surface oxygen functional groups was not the only factor. Nikiforidis *et al.* reported that a hydrophilic and inhomogeneous surface of CP was created after repetitive cyclic voltammetry (CV) in a Ce electrolyte.[42] Similar oxidation of the carbon electrodes by Ce(IV) would explain the observed wettability results. Ti is known to form polymer-like chains at higher concentrations in solution,[28]

Table 1 Atomic ratios (%) of carbon and oxygen from EDX

Elements	Pristine CP	HT CP	Pristine CF	HT CF
C	99.6 ± 0.1	99.6 ± 0.1	99.9 ± 0.0	95.8 ± 0.7
O	0.4 ± 0.0	0.4 ± 0.1	0.1 ± 0.0	4.2 ± 0.4

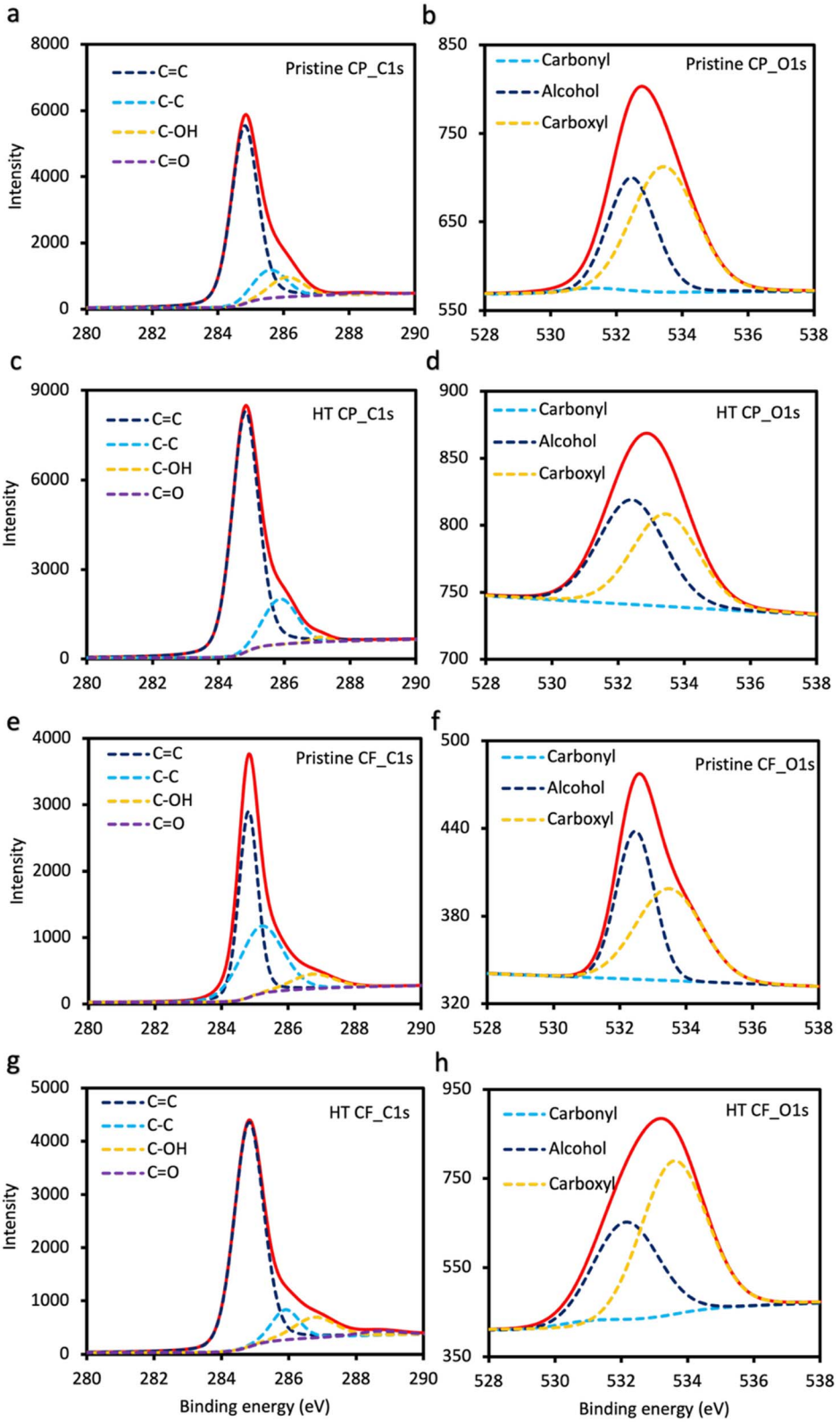

Fig. 2 XPS spectra of pristine CP (a and b), HT CP (c and d), pristine CF (e and f), and HT CF (g and h).

thereby affecting the viscosity and diffusion coefficients, and this would explain the lack of wettability on unfunctionalized surfaces. As reported by Ahmed *et al.*, the dynamic viscosity of Ti electrolytes in sulfuric acid has been found to increase from 1 cP to 2.4 cP when the H_2SO_4 concentration increased from 0 M to 4 M while keeping the Ti concentration constant at 0.5 M. When

Table 2 Percentage of different chemical bonds from XPS

		Pristine CP	HT CP	Pristine CF	HT CF
C 1s	Total	96.8 ± 0.2	98.5 ± 0.1	96.7 ± 0.2	90.5 ± 0.6
	C=C	76.2 ± 6.8	81.6 ± 5.0	51.4 ± 4.9	78.0 ± 5.9
	C–C	13.6 ± 4.2	17.3 ± 3.6	40.0 ± 5.2	9.8 ± 2.2
	C–OH	9.5 ± 3.3	1.1 ± 0.5	8.6 ± 2.5	10.1 ± 1.6
	C=O	0.7 ± 0.1	0.1 ± 0.1	0.0 ± 0.1	2.1 ± 0.9
O 1s	Total	2.8 ± 0.1	1.5 ± 0.0	2.6 ± 0.1	8.6 ± 0.5
	Carbonyl	2.5 ± 0.4	0.0 ± 0.1	0.0 ± 0.1	2.8 ± 1.2
	Alcohol	39.2 ± 3.8	53.0 ± 4.8	52.3 ± 5.3	37.7 ± 3.6
	Carboxyl	58.3 ± 2.4	47.0 ± 3.1	47.7 ± 3.4	59.5 ± 5.2

the Ti concentration was increased from 0.5 M to 5 M (with a constant 4 M H_2SO_4 concentration), the dynamic viscosity increased from 2.4 cP to 7.5 cP. Given the minimal variation in viscosity when the Ti concentration is kept at 0.5 M, we do not anticipate this playing a role in pressure drop, pumping losses, *etc.*[72] These results indicated that HT CF is the optimal electrode candidate for the Ti side, but the optimal surface for the Ce side could not be determined on the basis of surface wettability. Furthermore, since both surface characterization and the hydrophilicity test indicated minimal difference between CP and HT CP, we elected to use only CP for further experiments.

2.3 Electrochemical behavior of carbon electrodes in Ti and Ce electrolytes

In order to identify the optimum electrode configuration for Ti–Ce RFBs, CVs were recorded utilizing different types of carbon electrodes as the working electrode, as depicted in Fig. 4. As shown in Fig. 4a, both Ti reduction and Ti oxidation peaks were

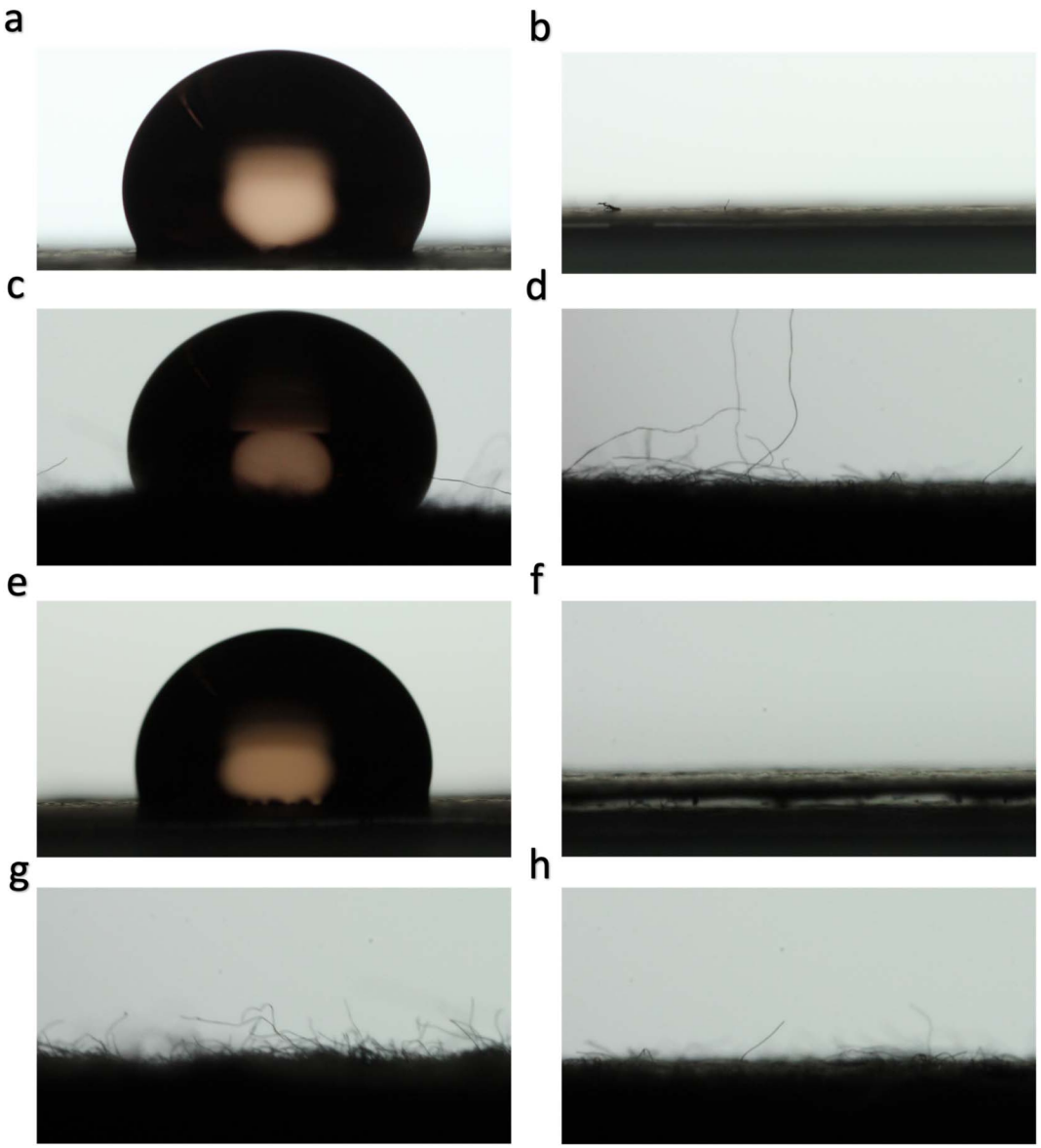

Fig. 3 Side views of a (a) Ti electrolyte droplet on pristine CP; (b) Ce electrolyte droplet on pristine CP; (c) Ti electrolyte droplet on pristine CF; (d) Ce electrolyte droplet on pristine CF; (e) Ti electrolyte droplet on HT CP; (f) Ce electrolyte droplet on HT CP; (g) Ti electrolyte droplet on HT CF; (h) Ce electrolyte droplet on HT CF.

Table 3 Contact angles of Ti & Ce electrolytes on CP & CF

Electrodes	Ti	Ce
Pristine CP	109.8° ± 5.6°	[a]
Pristine CF	113.6° ± 7.8°	[a]
HT CP	98.8° ± 4.0°	[a]
HT CF	[a]	[a]

[a] Found to spread and be absorbed into the porous electrode bulk with no discernible bubble formation.

observed only on HT CF, while pristine CF and CP lacked cathodic peaks, indicating poor activity for Ti reduction. Besides, the anodic peak potentials of pristine CF and CP were much more positive than that of HT CF (0.995 V and 0.798 V, respectively, *vs.* 0.075 V), and the corresponding peak currents were more than 20 times smaller than that of HT CF (5×10^{-4} A and 2×10^{-4} A, respectively, *vs.* 0.012 A), showing HT CF was much more active towards Ti oxidation. This improved activity is ascribed to the surface oxygen functional groups and increased surface roughness (and hence surface area) introduced by heat treatment. This agrees with previous studies in VRFBs,[43] Fe-RFBs,[44] Zn-RFBs,[45] and Cu-RFBs,[46] where electrode heat treatment was found to improve redox kinetics. Based on this, HT CF was selected as the negative electrode in Ti–Ce RFBs. In sharp contrast to its behavior with the Ti redox couple, HT CF showed no redox peaks in the case of the Ce electrolyte (except for a gradual increase in current at more anodic potentials, indicating the onset of oxygen evolution), while both anodic and cathodic peaks could be observed on pristine CF and pristine CP. However, each electrode exhibited different but equally desirable behavior: while both the anodic and cathodic peak currents on pristine CF was about 20 times that of CP (0.019 A *vs.* 0.002 A), indicating higher activity (translating to

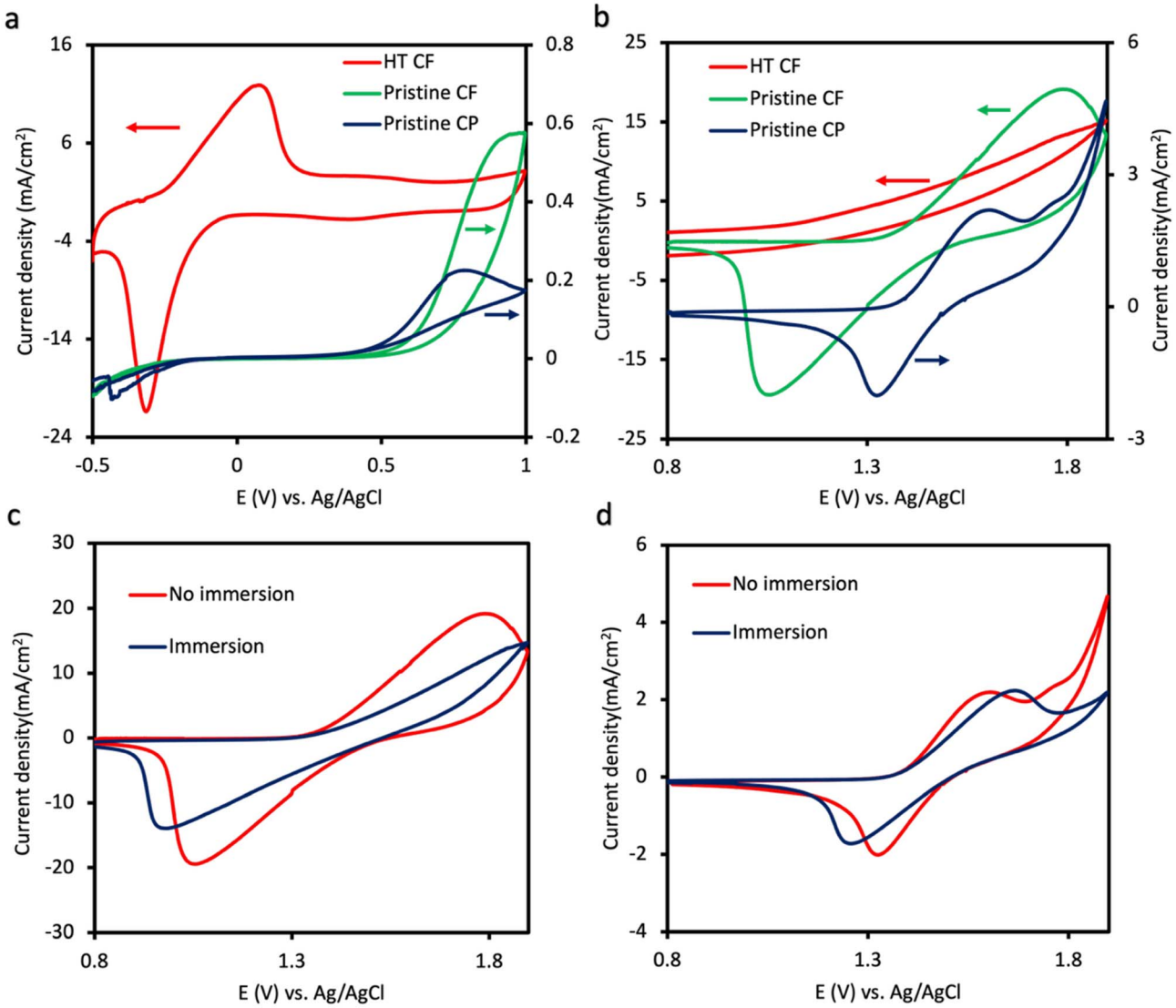

Fig. 4 Comparison of electrochemical responses with different electrodes in Ti/Ce electrolytes of 50% SOC at 2.5 mV s^{-1}. CVs of HT CF, pristine CF, and pristine CP in (a) Ti and (b) Ce electrolytes. CVs of (c) pristine CF and (d) pristine CP before and after being immersed in Ce electrolyte overnight.

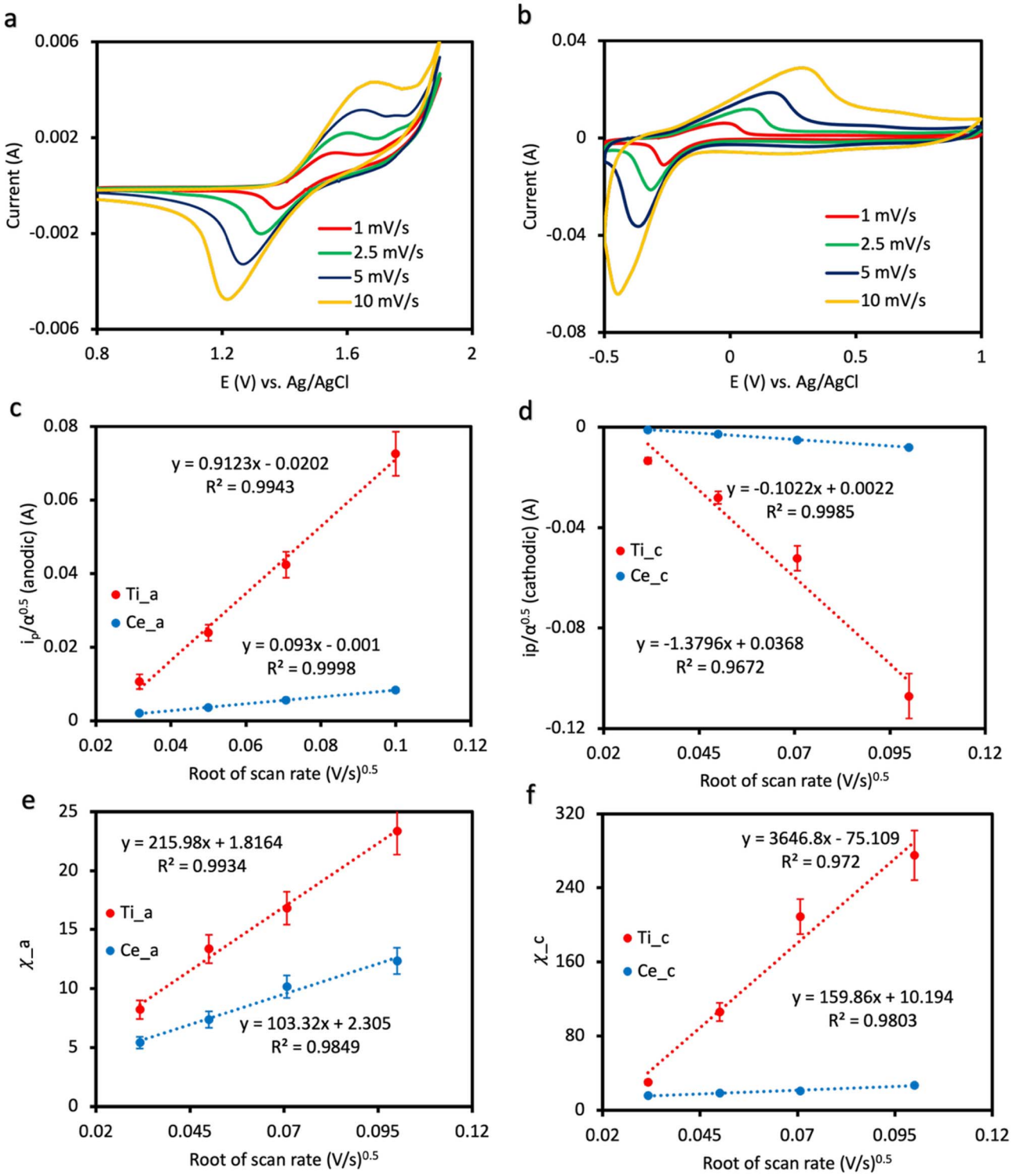

Fig. 5 Quantitative analysis of Ti & Ce reaction parameters. CVs of (a) CP in Ce electrolyte and (b) HT CF in Ti electrolyte at different scan rates. N–S plots of (c) anodic and (d) cathodic reactions. K–K plots of (e) anodic and (f) cathodic reactions.

higher operating current density in the RFB), the peak separation on CP was smaller than that of pristine CF (0.27 V *vs.* 0.73 V), indicating better reversibility and improved energy efficiency at the RFB cell level.[47] The higher peak current on pristine CF can be partially attributed to the higher surface area of CF than CP. But the fact that HT CF with even higher surface area exhibited negligible Ce redox activity indicated that this was not merely a surface area effect and that the lack of oxygen functional groups plays a positive role. The better reversibility on pristine CP is attributed to the stability of CP in Ce electrolyte, since Ce(IV) is a strong oxidizing agent.[48] We hypothesized that the formation of surface oxygen functional groups upon

Table 4 Electron transfer coefficients of Ti & Ce reactions

Scan rates (mV s^{-1})	Ti_α_a	Ti_α_c	Ce_α_a	Ce_α_c
1	0.334 ± 0.026	0.690 ± 0.037	0.464 ± 0.040	0.755 ± 0.052
2.5	0.294 ± 0.011	0.577 ± 0.034	0.368 ± 0.027	0.536 ± 0.041
5	0.196 ± 0.014	0.485 ± 0.021	0.315 ± 0.016	0.411 ± 0.020
10	0.157 ± 0.009	0.361 ± 0.028	0.270 ± 0.020	0.353 ± 0.029

Table 5 Mass transfer and kinetics parameters of Ti & Ce reactions

Parameters	Ce_CP_a	Ce_CP_c	Ti_HT CF_a	Ti_HT CF_c
Diffusion coefficient D_0 ($\times 10^{-4}$ cm^2 s)	0.48 ± 0.04	0.58 ± 0.18	46.0 ± 6.2	105.1 ± 11.2
Standard reaction rate constant k_0 ($\times 10^{-4}$ cm s^{-1})	9.1 ± 0.5	6.5 ± 0.1	42.7 ± 3.5	3.8 ± 0.5

immersion of pristine CF into the Ce electrolyte led to the relatively higher peak separation observed in the CVs. To test this hypothesis, CVs were compared before and after the electrodes were immersed in Ce electrolyte overnight. As depicted in Fig. 4c and d, both CF and CP degraded in terms of electrochemical performance (lower peak current and increased peak separation). However, the degradation of CF was more significant: the anodic peak was completely lost, and the cathodic peak current decreased by 26.3%. The shift in peak potentials was lower in the case of CP, along with no decrease in the anodic current and a 15% decrease in the cathodic current. Thus, CP was established to be more chemically stable to oxidation (in line with the observed lack of surface functionalization following thermal oxidation) and was determined to be a better candidate for the electrode on the Ce side, especially during long-term operation.

The CVs of CP in Ce electrolyte and HT CF in Ti electrolyte at different scan rates are shown in Fig. 5. The separation of anodic and cathodic peak potentials in Fig. 5a and b increased with scan rate and was much higher than 59 mV, indicating that both Ti and Ce redox reactions were irreversible.[47] Thus, the Nicholson–Shain (N–S) equation was used to correlate peak currents and scan rates, as shown below:

$$i_p = (2.99 \times 10^5) n^{3/2} \alpha^{1/2} A C_0 D_0^{1/2} \nu^{1/2} \quad (1)$$

where i_p is the peak current, n is the electron transfer number (1), α is the electron transfer coefficient, A is the surface area of the working electrode (1 cm^2), C_0 is the bulk concentration of active species (0.9 M), D_0 is the diffusion coefficient of active species, and ν is the scan rate.[49,50] Furthermore, the Klinger–Kochi (K–K) equation was used to calculate the standard reaction rate constant, as shown below:

$$k_0 \exp\left[\frac{\alpha n F}{RT}\left(E_p - E^0\right)\right] = 2.18\left[\frac{D\alpha n F \nu}{RT}\right]^{\left(\frac{1}{2}\right)} \quad (2)$$

where k_0 is the standard reaction rate constant, E_p is the potential value at peak current, E^0 is the standard potential, which was obtained from the average of anodic and cathodic peak potential values, R is the gas constant (8.314 J mol^{-1} K^{-1}), F is the Faraday constant (96 485 C mol^{-1}), and T is the temperature. Other symbols have the same meaning as in the N–S equation.[51]

The traditional N–S plot depicts i_p *vs.* $\nu^{1/2}$, whose slope is used to calculate D_0. The electron transfer coefficient, α, is usually taken to be 0.5 by convention, as shown in some previous studies.[52,53] However, it should be noted that it is only suitable to assume a value of 0.5 for reversible, elementary single-electron reactions.[47] As mentioned earlier, both Ti and Ce reactions were irreversible, meaning it is unreasonable to do so. In this case, the transfer coefficient, α, was quantitatively calculated using the following equation:[47]

$$\alpha = \frac{1.86RT}{F\left(E_p - E_{p/2}\right)} \quad (3)$$

where $E_{p/2}$ is the half-peak potential, which refers to the potential when the current reaches half of i_p. The results of α are listed in Table 4, demonstrating that the actual α values were significantly deviating from 0.5 as expected based on the irreversible nature of the reactions. Notably, the α values for the Ti redox couple were found to deviate more from the ideal value of 0.5 compared to values measured for the Ti redox couple in H_2SO_4 across a range of supporting electrolyte concentrations.[72] This was attributed to differences in solvation brought about by using MSA as the supporting electrolyte. The application of eqn (3) has been proven to be an effective and accurate way to determine the charge transfer coefficient,[54] and the observation that α values calculated from eqn (3) was inversely correlated with the scan rate was in agreement with that study's conclusions. This phenomenon was understood to be a result of the potential-dependent nature of transfer coefficients at high overpotentials. The Butler–Volmer model assumes an exponential relationship between charge transfer rate and electrode overpotential regardless of how far it is from equilibrium, which is not consistent with the modern understanding of charge transfer.[55,56] Based on this, the original N–S and K–K equations were slightly modified by moving α from the right- to the left-hand side:

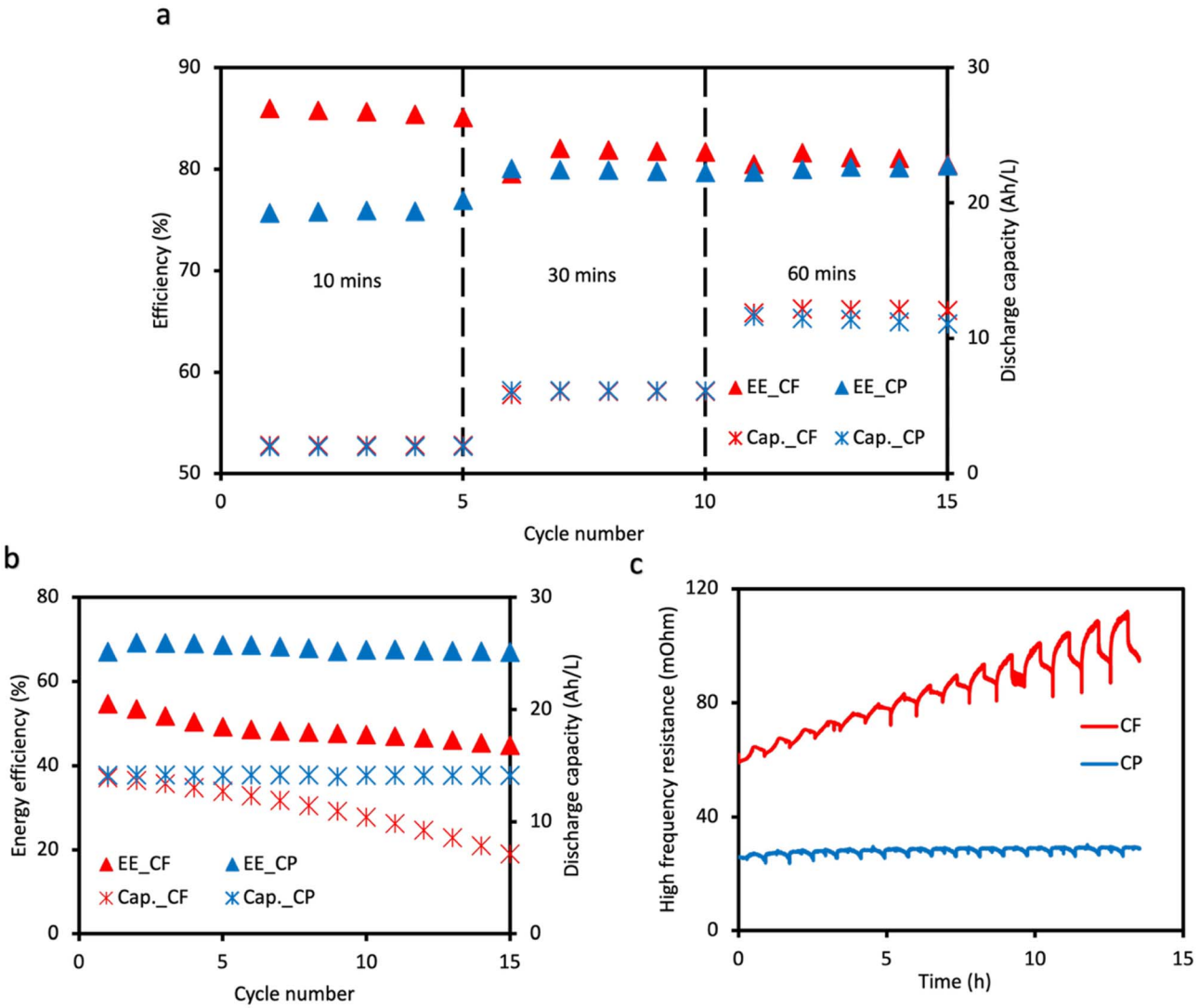

Fig. 6 Ti–Ce RFB performance. Comparison between CF and CP working as electrodes on the Ce side under (a) galvanostatic 50 mA cm^{-2} with different charge/discharge durations and (b) galvanostatic 150 mA cm^{-2} plus potentiostatic protocol at 2/1 V for charge/discharge. (c) HFR evolution comparison between CF and CP working as electrodes on the Ce side with galvanostatic 150 mA cm^{-2} plus potentiostatic protocol at 2/1 V for charge/discharge.

$$i_p/\alpha^{1/2} = (2.99 \times 10^5) n^{3/2} A C_0 D_0^{1/2} \nu^{1/2} \quad (4)$$

by defining

$$\chi = \exp\left[\frac{\alpha n F}{RT}(E_p - E^0)\right] \Big/ \alpha^{1/2} \quad (5)$$

the K–K equation turns into

$$\chi = \frac{2.18}{k_0}\left[\frac{DnF\nu}{RT}\right]^{\left(\frac{1}{2}\right)} \nu^{1/2} \quad (6)$$

Thus, the diffusion coefficient, D_0, and standard reaction rate constant, k_0, were obtained from the slope of the N–S plot ($i_p/\alpha^{1/2}$ *vs.* $\nu^{1/2}$) and the K–K plot (χ *vs.* $\nu^{1/2}$), respectively. The N–S and K–K plots are depicted in Fig. 5, and the results for D_0 and k_0 are listed in Table 5. The diffusion coefficients of Ti on HT CF were more than two orders higher than those of Ce on CP. The porous nature of HT CF was expected to result in the measured diffusion coefficient being an effective diffusion coefficient including the effect of constrained diffusion within the pores of HT CF. Thus, the fact that the effective diffusion coefficient of Ti is still higher than that of Ce on a much less porous CP electrode indicates that Ce is transport limited. The measured diffusion coefficients of Ce were also more than one order of magnitude higher than values obtained from some previous studies using dilute Ce solutions (0.01 to 0.2 M) and with sulfuric acid supporting electrolytes.[57,58] The diffusion coefficient of active species is strongly dependent on the concentration and type of supporting electrolyte and thus only broad comparisons of diffusion coefficient trends would be strictly valid when comparing measurements made with electrolytes having different supporting electrolytes. These studies also used a non-porous, planar electrode, and thus the difference in

calculated diffusion coefficients also reflects the difference between the geometric and electrochemically active surface area (ECSA) of the electrode. The geometric area and ECSA would be very close to each other in the planar model electrodes, while they differ significantly (even by 10–100 times) in practical, porous electrodes. Since diffusion within pores must be considered, a film diffusion coefficient was proposed to reflect the difference from bulk diffusion by a partition coefficient (partitioning between the bulk and the film formed on the pore walls) in a porous electrode system.[73] This difference existed on both sides making the results quantitatively comparable. We strongly recommend that these fundamental electrochemical measurements should be carried out using the actual electrode material that is intended to be used in the RFB. This will ensure that these measurements can actually serve as useful guides for RFB engineering. We measured the diffusion coefficients and rate constants on the same HT CF and CP that are also used as electrodes in the Ti–Ce RFBs; thus, this measurement is much more representative of the conditions encountered in actual operation. The ECSA can be calculated from the double-layer capacitance.[59] The N–S equation itself has also been used to calculate the ECSA, as long as an independent measure of the diffusion coefficient is available.[60] CVs of CP and HT CF were measured within the non-faradaic region to determine the double layer capacitance, C_{dl} (Fig. S2 and Table S2). With a geometrical surface area of 1 cm^2, the specific capacitance, C_s, of HT CF was measured to be ~4700× that of CP. This improved C_s directly correlates to higher measured reaction rates over an electrode of the same geometric area even though the rate constant is unchanged. Based on the discussion above, the D_0 and k_0 numbers measured here can be defined as the "nominal" values because they accurately reflect the different effects of HT CF and CP with a common geometrical surface area. Similarly, the reaction rate constants listed in Table 5 should be examined with this understanding of the effect of electrode surface area. Notably, the rate constant for Ce reduction was found to be lower than that for Ti oxidation, while Ce oxidation was faster than Ti reduction. Thus, Ce was expected to be the rate limiting electrode during discharge, while Ti was expected to be rate limiting during charge. To verify this, polarization curves of symmetric cells utilizing Ce or Ti electrolyte of 50% SOC were compared, as depicted in Fig. S3. The overpotential of the Ce side was higher than that of Ti during discharge and *vice versa* during charge, which supported the finding that Ce was rate limiting during discharge and Ti during charge.

2.4 Ti–Ce RFB performance

To verify the advantage of the asymmetric electrode configuration, pristine CF and CP were used separately as positive electrodes in Ti–Ce RFBs to test the performance, as depicted in Fig. 6. Only positive electrodes were varied, as the Ti electrolyte was found to not even wet the CP surface, as shown in Section 2.1. Fig. 6a shows the performance at a relatively low current density (50 mA cm^{-2}) with different cycling durations. Over 10-minute cycles, the energy efficiency (EE) of CF was significantly higher than that of CP (85.6% *vs.* 76.0%), as the much higher active surface area of CF compared to CP provided more active sites for the Ce reaction, thus promoting the reaction rate. However, as the cycling experiment proceeded, EE of CF and CP gradually decreased and increased, respectively, and reached the same level in the 60-minute cycle stage (81.0%). As shown in Fig. S4, the polarization losses of CF were gradually increased, while those of CP remained constant. The degradation of CF during RFB operation was consistent with the stability test in Ce(IV) electrolytes, *i.e.*, the structure of CF was destroyed by the highly oxidizing nature of Ce(IV), leading to lower EE. In

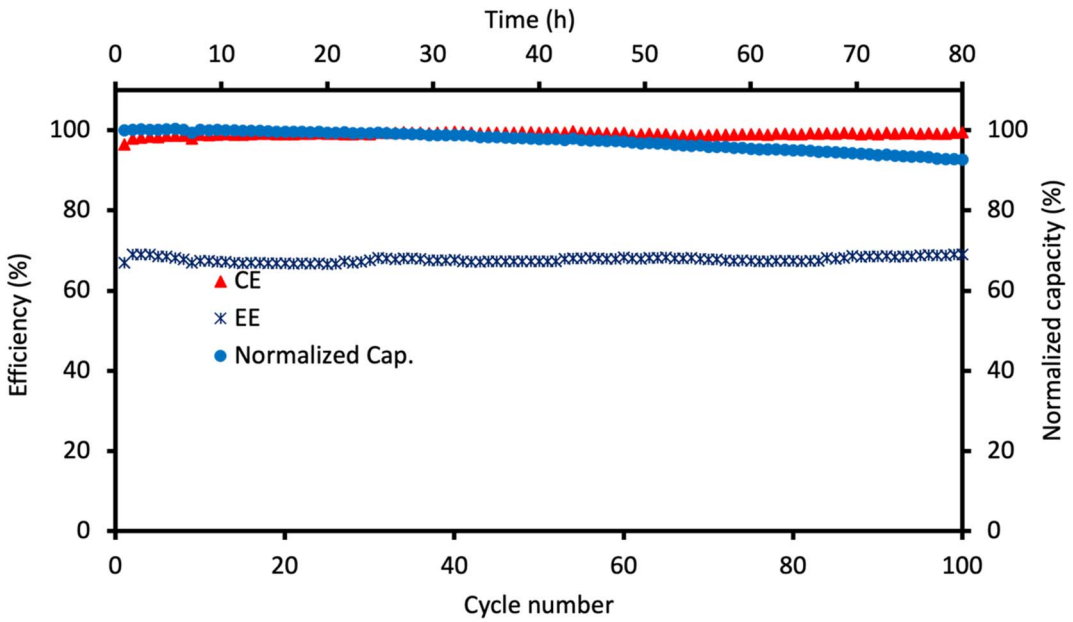

Fig. 7 Long-term cycling performance of the optimized RFB cell with CP/HT CF as the electrode on the Ce/Ti side with galvanostatic 150 mA cm^{-2} plus potentiostatic protocol at 2/1 V for charge/discharge.

Table 6 Comparison of Ce RFB performance between this work and previous studies

RFB type	Positive electrolyte	Negative electrolyte	Highest operating current density (mA cm^{-2})	Highest discharge voltage (V)	EE (%)	# of finished cycles	Reference
Zn–Ce	0.8 M $Ce(CH_3SO_3)_3$ in 4 M MSA	1.5 M $Zn(CH_3SO_3)_2$ in 1 M MSA	50	1.77	59.3	57	67
Pb–Ce	1 M $Ce(CH_3SO_3)_3$ in 1 M MSA	1.5 M $Pb(CH_3SO_3)_2$ in 1 M MSA	10	1.67	79	800	21
V–Ce	0.9 M $Ce(CH_3SO_3)_3$ in 4 M MSA	0.9 M $VOSO_4$ in 5.8 M MSA	100	1.25	51	100	22
Non-aqueous V–Ce	0.05 M $[Ce(Py–O)_8][Tf_2N]_3$[a] in 0.5 M $TEABF_4$/ACN[b]	0.05 M $V(acac)_3$[c] in 0.5 M $TEABF_4$/ACN[b]	1	2.1	< 75	50	68
Fe–Ce	0.1 M $Ce(SO_4)_2$ in 1 M H_2SO_4	0.05 M $FeSO_4$ in 1 M H_2SO_4	25	0.8	66.2	100	69
Ti–Ce	0.9 M $Ce(CH_3SO_3)_3$ in 4 M MSA	0.9 M $TiOSO_4$ in 3.8 M MSA	150	1.4	67.8	100	This work

[a] Cerium bis(trifluoromethylsulfonyl)imide. [b] Tetraethylammonium tetrafluoroborate/acetonitrile. [c] Vanadium acetylacetonate.

contrast, it was interesting to find that, since CP was resilient to Ce(IV), the EE of CP was promoted over time, pointing to possible CP activation by Ce(IV) during the experiment to become more favorable for the Ce reaction. The difference in RFB performance between CF and CP was more significant at high current density (150 mA cm^{-2}), as shown in Fig. 6b. The average EE of CF was only 48.6%, while that of CP was 68.1%. Moreover, both EE and discharge capacity decreased over cycling when CF was used as the electrode of the Ce side. It is clearly shown in Fig. 6c that the degradation of CF during cycling increased high frequency resistance (HFR) from 60 to 110 mOhm, while HFR of CP stayed below 30 mOhm. Higher HFR resulted in greater ohmic losses, which lowered the EE, especially when the applied current density was high. To identify the source of the increase in HFR on the untreated CF, characterization was performed on CP and CF at the Ce side after the cycling experiment. As shown in Fig. S5 (and compared to the SEM images in Fig. 1), the surface morphology of CP was unchanged after cycling but CF showed significant surface roughening. The EDX results listed in Table S3 clearly show the dramatic increase (compared to CP) in surface oxygen on CF after cycling, and this indicates that oxidative degradation of untreated CF resulted in increased charge transfer resistance and decreased performance. Thus, CP was concluded to be the better choice of electrode for the Ce side, validating our choice based on CV measurements.

The generally accepted opinion about HFR in RFBs is that it is dominated by the ionic resistance of the ion exchange membrane.[61–63] The contact resistance of other components in RFBs, especially that from porous CF, has been studied in some previous studies. A more compressed CF would result in a lower HFR, with possible destruction of the mechanical properties of CF and increase in pressure drop. The effect of compression ratio on this tradeoff was reported for VRFBs, with the optimum compression ratio lying within a wide range from 25% to 60%.[64–66] To identify the optimum compression ratio for CF on the Ti side, three different values (25%, 48%, and 53%) were selected based on the different types of gaskets during cell assembling, and the results are shown in Fig. S6, SI. As the compression ratio was increased from 25% to 48%, the HFR decreased from 50 mOhm to 30 mOhm, and the EE correspondingly increased from 63.5% to 67.7%. A further increase in the compression ratio became difficult, as CF tended to break, and the HFR from other components (*e.g.*, membrane and electrolytes) remained unchanged. Our previous study utilized a hydraulic–electrical analogous model to reveal that when the compression was increased from 10 to 40%, the hydraulic power loss was promoted by approximately 40%.[74] The EE further increased to 69.2% when the compression ratio was increased to 53%, while the change of HFR was negligible, indicating that the HFR optimum had been reached. Based on this, the compression ratio of HT CF on the Ti side should be maintained at around 50% to yield the best performance.

The long-term cycling result with this optimal configuration (a CP electrode on the Ce side and a 50% compressed HT CF electrode on the Ti side) over the entire SOC range is depicted in Fig. 7. Notably, this optimization effort allowed us to increase

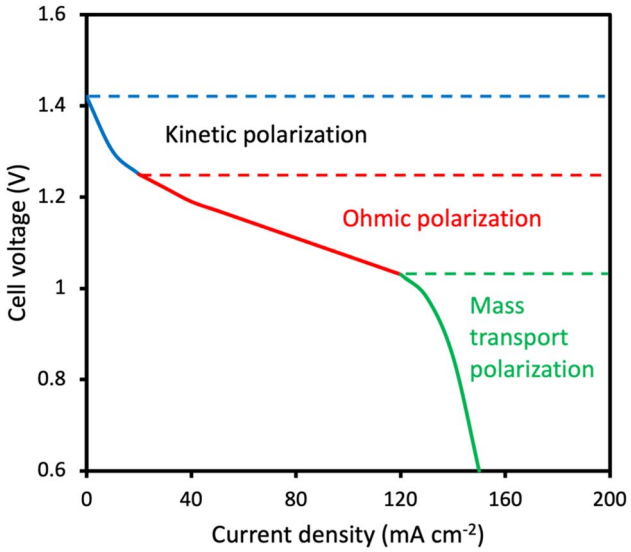

Fig. 8 Illustration of the polarization curve during RFB operation.

the operating current density from 100 to 150 mA cm^{-2} over 100 cycles in 80 h. The average coulombic efficiency and EE were 99.1% and 67.8%, respectively, and about 93% of the initial discharge capacity was retained at the end of cycling. The cycling was conducted with a galvanostatic plus potentiostatic protocol, and some irreversible side reactions (*e.g.*, hydrogen evolution) might happen when the cell was held at a high potential (2 V). The theoretically upper limit of the charge capacity of the $(n + 1)$th cycle was the same as the discharge capacity of the nth cycle, which was lower than the charge capacity of the nth cycle due to the fact that the coulombic efficiency was close but never equal to 100%. Therefore, the discharge capacity would inevitably decrease overtime. Additionally, we observed almost no capacity fade over >200 cycles when the range of SOC over which we cycled was narrowed by imposing a time limit on the charge and discharge cycles, as shown in Fig. S8. The discharge voltage reached 1.4 V according to charge–discharge curves depicted in Fig. S7. The performance reported here is better than most other types of RFBs utilizing Ce, *e.g.*, Zn–Ce,[67] Pb–Ce,[21] V–Ce RFBs,[22] and non-aqueous Ce RFBs,[68] as summarized in Table 6. The operating

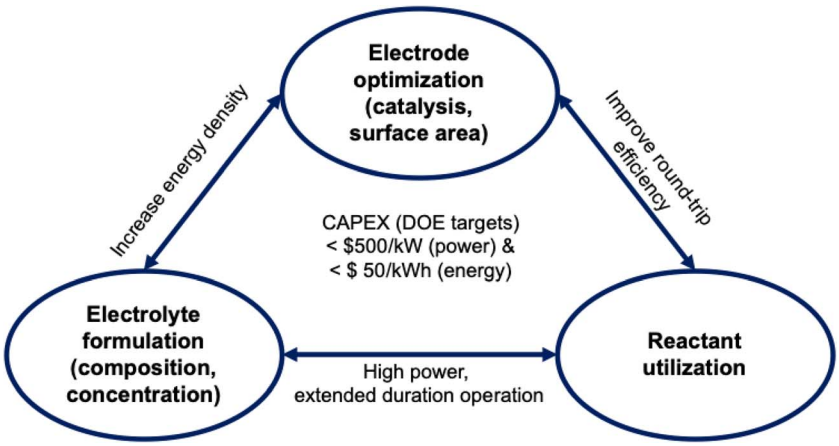

Fig. 9 Interlinks between performance metrics and design parameters.

Table 7 Relationship matrix between RFB performance metrics and design parameters

Affected performance parameter	RFB design variable	Governing equation and control variable	Design modifications examined
Energy efficiency (indirectly affected through RFB cell resistance)	(1) Electrode thickness	(1) $\sigma_{electrode} = \frac{t_{electrode}}{R_{HFR} A_{electrode}}$	(1) Varying electrode thickness and porosity
	(2) Separator thickness	(2) $\sigma_{separator} = \frac{t_{separator}}{R_{HFR} A_{separator}}$	(2) Thinner separator, reinforced separator
	(3) Electrolyte conductivity	(3) $\kappa_{electrolyte} = \frac{L}{R_{electrolyte} A} = z_+ v_+ C_{electrolyte} (\lambda_+ + \lambda_-)$	(3) Electrolyte additives, mixed supporting electrolytes
Power density	(1) Electrode surface area	(1) $i = nFAkC$	(1) Varying electrode material and thickness
	(2) Electrode active surface modification	(2) $k = k_0 \exp\left(-\frac{\alpha F \eta}{RT}\right)$	(2) Electrode pretreatment (thermal, H_3PO_4 immersion, *aqua regia* immersion) and/or Bi electrodeposition

current density of this work was the highest compared to previous studies, and a high current density is typically not beneficial to energy efficiency since the ohmic polarization is increased. Despite this, the energy efficiency of this work is still higher than most previous studies. Furthermore, the concentration applied in this study is also the highest among all the studies, indicating a great advantage of promoting capacity storage and lowering capital cost. In a recent study, the Ti compound was decorated on CF to enhance the kinetics of the Ce redox reaction, and a Fe–Ce RFB was developed based on this idea.[69] The EE from this study was 66.2% at 25 mA cm^{-2}, which was close to that achieved in this study at 150 mA cm^{-2}. Thus, the Ti–Ce RFB presented here shows great potential for commercialization and scaling up.

2.4.1 Generalized design optimization approach for RFBs. During RFB operation, activation polarization, ohmic polarization, and concentration polarization dominate sequentially as current density increases, as shown in Fig. 8. The overpotential induced by each type of polarization includes the contribution from both cathodic and anodic sides. For example, during discharge, Ce and Ti undergo cathodic and anodic reactions, respectively, and the activation polarization could be expressed as follows:

$$\eta_{act\_c} = \frac{RT}{\alpha_{Ce\_c}F}\ln(i) - \frac{RT}{\alpha_{Ce\_c}F}\ln(i_{0\_Ce}) \quad (7)$$

$$\eta_{act\_a} = \frac{RT}{\alpha_{Ti\_a}F}\ln(i) - \frac{RT}{\alpha_{Ti\_a}F}\ln(i_{0\_Ti}) \quad (8)$$

where i_0 is the exchange current density. Similarly, the ohmic overpotential could be expressed as

$$\eta_{ohmic\_c} = iA_{Ce}\frac{1}{G_{Ce}} \quad (9)$$

$$\eta_{ohmic\_a} = iA_{Ti}\frac{1}{G_{Ti}} \quad (10)$$

where A and G are the electrode surface area and electrolyte conductance, respectively.

The polarization curve presented above is typical of RFBs and can be used as a general diagnostic tool to identify losses and areas for improvement. Fig. 9 depicts the interlinked RFB design parameters (*e.g.*, electrode thickness, separator thickness, *etc.*) and its effects on RFB performance parameters. Table 7 provides suggested modifications to the RFB design depending on the performance limiting design parameter identified using the polarization curve.

3. Conclusion

A Ti–Ce RFB with an asymmetric electrode configuration was proposed and developed in this study guided by a series of broadly applicable fundamental surface and electrochemical characterization techniques. It is shown that using the actual electrode and electrolyte employed in a RFB to also measure electrochemical characteristics such as the diffusion coefficient and rate constant leads to better agreement with cell level results and avoids the pitfalls introduced by idealized dilute electrolytes and model, non-porous, planar electrodes. By evaluating and downselecting electrode candidates based on surface wettability and electrochemical performance (reversibility and redox reaction rates), traditional thermally treated CF was utilized as the negative electrode, while CP was selected as the positive electrode, as it was more resilient to the oxidizing nature of Ce(IV). This cell was further optimized by adjusting the CF compression ratio to balance reduced ohmic losses and increased pressure drop. This optimized RFB operated at 150 mA cm^{-2} and delivered stable coulombic and energy efficiencies of 99.1% and 67.8%, respectively, and a capacity retention of 93% by the end of 100 cycles – a significant improvement across multiple metrics compared to other Ce-based RFBs. The demonstrated Ti–Ce RFB presents great potential for the development of economically and environmentally friendly inorganic RFBs. The approach presented herein can also be generalized to improve the performance of other RFBs.

4. Experimental section

4.1 Preparation of materials

Titanium oxysulfate ($TiOSO_4$) and MSA were purchased from Sigma-Aldrich; cerium carbonate ($Ce_2(CO_3)_3$) was purchased from Treibacher Industries A. G. Ti electrolyte was made by dissolving $TiOSO_4$ in deionized water first, and then the corresponding amount of MSA was added; Ce electrolyte was made by mixing $Ce_2(CO_3)_3$ and deionized water to form a slurry first, and then MSA was added slowly to react with $Ce_2(CO_3)_3$. The slurry was mixed using a magnetic bar rotated at a low speed (100 rpm). After every 1 mL of MSA was added, no more MSA was added until the reaction was completed and no CO_2 bubbles were observed. CP (AvCarb MGL 190, Fuel Cell Store) and CF (GFA 6, SGL Group) were heat treated in a muffle furnace at 500 °C for 8 h under an air atmosphere. The optimum treatment temperature was concluded based on a screening at different temperatures, as depicted in Fig. S10. As the temperature increased from 400 to 550 °C, the EE first increased from 47.7% to 66.9% at 500 °C and then slightly decreased. The synthesis of the quaternized cardo-poly(ether ketone)-based anion exchange membrane functionalized with trimethylamine (QPEK-C-TMA AEM) followed the same procedure as in one of our previous studies.[70,71]

4.2 Electrochemical methods

Cyclic voltammetry (CV) was conducted with WaveNowXV Potentiostat Bundles (PINE Research), and a three-electrode system was set up utilizing an Ag/AgCl reference electrode, a platinum wire counter electrode, and a CP or CF working electrode. The geometrical surface area of the working electrode was 1 cm^2 for all tests. The scan range for Ti and Ce was −0.5 to 1 V and 0.8 to 1.9 V *vs.* Ag/AgCl, respectively, and four different scan rates, 1, 2.5, 5, and 10 mV s^{-1}, were used for further calculations using the N–S and K–K equations. The Ti and Ce electrolytes with 50% state of charge (SOC) were obtained by running a half-charge protocol in a Ti–Ce RFB and then diluted 10 times using the same concentration of

MSA on each side. The reason was that the current from the CV experiment would be extremely large with the original concentration due to the much higher reaction activity of CP and CF compared with the more commonly used working electrode, glassy carbon, which would interfere with the identification of the peak current position and value.

4.3 Characterization methods

SEM/EDX was conducted with an environmental scanning electron microscope (Thermofisher Quattro S ESEM) equipped with an Oxford AzTec Energy Dispersive X-ray Spectrometer (EDXS). The acceleration voltage was 5 kV, and the working distance was around 10 mm. XPS was conducted with a Physical Electronics 5000 VersaPhobe II scanning ECSA microprobe. A broad survey spectrum was collected before fine scans for each element. The contact angle picture was captured with a homemade goniometer mainly composed of a camera and a lighting background, and the contact angle was then measured using ImageJ.

4.4 RFB tests

Ti–Ce RFBs were operated with an 857 Redox Flow Cell Test System (Scribner). The geometrical surface area of negative and positive electrodes was 25 cm^2 (5 × 5 cm). The volume of electrolyte on each side was 100 mL, and it was pumped through the cell with a flow rate of 140 mL min^{-1}. The 50 mA cm^{-2} protocol was purely galvanostatic for both charge and discharge processes with different durations (10, 30, and 60 min), and the battery was operated for 5 cycles at each time length. The 150 mA cm^{-2} protocol was galvanostatic plus potentiostatic to fully charge and discharge the system. During charging, the cell was operated at a current of 150 mA cm^{-2} until the potential reached the cutoff value (2 V), and then the potential was held at this level until the current decreased to 20 mA cm^{-2}. Likewise, −150 mA cm^{-2} was applied at the beginning of discharge until the potential decreased to the cutoff value (1 V), followed by a potentiostatic stage at this potential until the current increased to −20 mA cm^{-2}. The protocol for polarization curve measurements can be found in Section 2, SI.

Conflicts of interest

The authors currently have no financial interests that may be perceived to influence the conclusions presented in this work. Some of the authors are seeking intellectual property protections on aspects of one or more technologies described in this report through the Office of Technology and Management (OTM) at Washington University in St. Louis (WUSTL).

Data availability

The raw data are available from the corresponding author upon reasonable request.

All of the data associated with these studies are represented in the manuscript and its supplementary information (SI). Supplementary information: XPS survey data, CVs in non-Faradaic region, polarization curves, SEM of electrodes after cycling experiment, charge–discharge curves, Ti–Ce RFB performance with different CF compression ratios, and properties of CP and CF. See DOI: https://doi.org/10.1039/d5se01171j.

Acknowledgements

This work was supported by the Advanced Research Projects Agency-Energy (ARPA-E), the US Department of Energy under award no. DE-AR0000768 as part of the Integration and Optimization of Novel Ion Conducting Solids (IONICS) program and the McKelvey School of Engineering, Washington University in St. Louis and the Roma B. & Raymond H. Wittcoff Distinguished University Professorship. Jing Xie wants to thank Dr Huafang Li from the Institute of Materials Science & Engineering at Washington University in St. Louis for the help in terms of materials characterization.

References

1 S. Chen, M. Zhang, P. Zou, B. Sun and S. Tao, Historical Development and Novel Concepts on Electrolytes for Aqueous Rechargeable Batteries, *Energy Environ. Sci.*, 2022, **15**(5), 1805–1839, DOI: 10.1039/d2ee00004k.
2 K. Zou, W. Deng, D. S. Silvester, *et al.*, Carbonyl Chemistry for Advanced Electrochemical Energy Storage Systems, *ACS Nano*, 2024, **18**(31), 19950, DOI: 10.1021/acsnano.4c02307.
3 Y. Liang, H. Dong, D. Aurbach and Y. Yao, Current Status and Future Directions of Multivalent Metal-ion Batteries, *Nat. Energy*, 2020, **5**(9), 646–656, DOI: 10.1038/s41560-020-0655-0.
4 M. Lin, M. Gong, B. Lu, *et al.*, An Ultrafast Rechargeable Aluminium-ion Battery, *Nature*, 2015, **520**(7547), 324–328, DOI: 10.1038/nature14340.
5 B. Li, Z. Nie, M. Vijayakumar, *et al.*, Ambipolar Zinc-Polyiodide Electrolyte for a High-Energy Density Aqueous Redox Flow Battery, *Nat. Commun.*, 2015, **6**(1), 6303, DOI: 10.1038/ncomms7303.
6 A. Hollas, X. Wei, V. Murugesan, *et al.*, A Biomimetic High-capacity Phenazine-based Anolyte for Aqueous Organic Redox Flow Batteries, *Nat. Energy*, 2018, **3**(6), 508–514, DOI: 10.1038/s41560-018-0167-3.
7 Z. Li and Y. Lu, Polysulfide-based Redox Flow Batteries With Long Life and Low Levelized Cost Enabled by Charge-reinforced Ion-selective Membranes, *Nat. Energy*, 2021, **6**(5), 517–528, DOI: 10.1038/s41560-021-00804-x.
8 M. Rychcik and M. Skyllas-Kazacos, Characteristics of a New All-vanadium Redox Flow Battery, *J. Power Sources*, 1988, **22**(1), 59–67, DOI: 10.1016/0378-7753(88)80005-3.
9 H. R. Jiang, J. Sun, L. Wei, M. C. Wu, W. Shyy and T. S. Zhao, A High Power Density and Long Cycle Life Vanadium Redox Flow Battery, *Energy Storage Mater.*, 2019, **24**, 529–540, DOI: 10.1016/j.ensm.2019.07.005.
10 K. E. Rodby, R. L. Jaffe, E. A. Olivetti and F. R. Brushett, Materials Availability and Supply Chain Considerations for Vanadium in Grid-scale Redox Flow Batteries, *J. Power Sources*, 2023, **560**, 232605, DOI: 10.1016/j.jpowsour.2022.232605.

11 L. Tang, P. Leung, M. R. Mohamed, *et al.*, Capital Cost Evaluation of Conventional and Emerging Redox Flow Batteries for Grid Storage Applications, *Electrochim. Acta*, 2023, **437**, 141460, DOI: 10.1016/j.electacta.2022.141460.
12 R. M. Darling, K. G. Gallagher, J. A. Kowalski, S. Ha and F. R. Brushett, Pathways to Low-Cost Electrochemical Energy Storage: A Comparison of Aqueous and Nonaqueous Flow Batteries, *Energy Environ. Sci.*, 2014, **7**(11), 3459–3477, DOI: 10.1039/C4EE02158D.
13 R. M. Darling, Techno-Economic Analyses of Several Redox Flow Batteries Using Levelized Cost of Energy Storage, *Curr. Opin. Chem. Eng.*, 2022, **37**, 100855, DOI: 10.1016/j.coche.2022.100855.
14 S. Sankarasubramanian and V. Ramani, Redox flow battery, *US Pat.*, 11177497, 2021.
15 S. Sankarasubramanian, Y. Zhang, C. He, T. Gregory and V. Ramani, An Aqueous, Electrode-Decoupled Redox-Flow Battery for Long Duration Energy Storage, preprint, 2021, DOI: 10.21203/rs.3.rs-150474/v1.
16 K. Binnemans, P. T. Jones, K. Van Acker, B. Blanpain, B. Mishra and D. Apelian, Rare-Earth Economics: The Balance Problem, *JOM*, 2013, **65**(7), 846–848, DOI: 10.1007/s11837-013-0639-7.
17 H. Tsurugi and K. Mashima, Renaissance of Homogeneous Cerium Catalysts with Unique Ce(IV/III) Couple: Redox-Mediated Organic Transformations Involving Homolysis of Ce(IV)–Ligand Covalent Bonds, *J. Am. Chem. Soc.*, 2021, **143**(21), 7879–7890, DOI: 10.1021/jacs.1c02889.
18 A. Paulenova, S. E. Creager, J. D. Navratil and Y. Wei, Redox Potentials and Kinetics of the Ce3+/Ce4+ Redox Reaction and Solubility of Cerium Sulfates in Sulfuric Acid Solutions, *J. Power Sources*, 2002, **109**(2), 431–438, DOI: 10.1016/S0378-7753(02)00109-X.
19 R. M. Spotnitz, R. P. Kreh, J. T. Lundquist and P. J. Press, Mediated Electrosynthesis with Cerium (IV) in Methanesulphonic Acid, *J. Appl. Electrochem.*, 1990, **20**(2), 209–215, DOI: 10.1007/BF01033596.
20 P. K. Leung, C. Ponce-de-León, F. J. Recio, P. Herrasti and F. C. Walsh, Corrosion of the Zinc Negative Electrode of Zinc–Cerium Hybrid Redox Flow Batteries in Methanesulfonic Acid, *J. Appl. Electrochem.*, 2014, **44**(9), 1025–1035, DOI: 10.1007/s10800-014-0714-y.
21 Z. Na, S. Xu, D. Yin and L. Wang, A Cerium–Lead Redox Flow Battery System Employing Supporting Electrolyte of Methanesulfonic Acid, *J. Power Sources*, 2015, **295**, 28–32, DOI: 10.1016/j.jpowsour.2015.06.115.
22 S. Sankarasubramanian, Y. Zhang and V. Ramani, Methanesulfonic Acid-Based Electrode-Decoupled Vanadium–Cerium Redox Flow Battery Exhibits Significantly Improved Capacity and Cycle Life, *Sustainable Energy Fuels*, 2019, **3**(9), 2417–2425, DOI: 10.1039/C9SE00286C.
23 M. Sarraf, E. R. Ghomi, S. Alipour, S. Ramakrishna and N. L. Sukiman, A State-of-the-Art Review of the Fabrication and Characteristics of Titanium and Its Alloys for Biomedical Applications, *Bio-Des. Manuf.*, 2022, **5**(2), 371–395, DOI: 10.1007/s42242-021-00170-3.
24 V. Anil Kumar, R. K. Gupta, M. J. N. V. Prasad and S. V. S. Narayana Murty, Recent Advances in Processing of Titanium Alloys and Titanium Aluminides for Space Applications: A Review, *J. Mater. Res.*, 2021, **36**(3), 689–716, DOI: 10.1557/s43578-021-00104-w.
25 P. Pushp, S. M. Dasharath and C. Arati, Classification and Applications of Titanium and Its Alloys, *Mater. Today: Proc.*, 2022, **54**, 537–542, DOI: 10.1016/j.matpr.2022.01.008.
26 C. Yang, H. Wang, S. Lu, *et al.*, Titanium Nitride as an Electrocatalyst for V(II)/V(III) Redox Couples in All-Vanadium Redox Flow Batteries, *Electrochim. Acta*, 2015, **182**, 834–840, DOI: 10.1016/j.electacta.2015.09.155.
27 L. Zhang, Y. Jiang, H. Wang, P. Qian, J. Sheng and H. Shi, Sulfonated Poly (Ether Ketone)/Sulfonated Titanium Dioxide Hybrid Membrane with High Selectivity and Good Stability for Vanadium Redox Flow Battery, *J. Energy Storage*, 2022, **45**, 103705, DOI: 10.1016/j.est.2021.103705.
28 S. I. U. Ahmed, M. Shahid and S. Sankarasubramanian, Aqueous Titanium Redox Flow Batteries—State-of-the-Art and Future Potential, *Front. Energy Res.*, 2022, **10**, 1021201, DOI: 10.3389/fenrg.2022.1021201.
29 L. Qiao, M. Fang, S. Liu, H. Zhang and X. Ma, New-Generation Iron–Titanium Flow Batteries with Low Cost and Ultrahigh Stability for Stationary Energy Storage, *Chem. Eng. J.*, 2022, **434**, 134588, DOI: 10.1016/j.cej.2022.134588.
30 M. Nan, M. Wu, Y. Liu, L. Qiao, H. Zhang and X. Ma, Boosting the Areal Capacity of Titanium-Manganese Single Flow Battery by Fe^{2+}/Fe^{3+} Redox Mediator, *Small Methods*, 2023, **7**(1), 2201266, DOI: 10.1002/smtd.202201266.
31 W. H. Wang and X. D. Wang, Investigation of Ir-Modified Carbon Felt as the Positive Electrode of an All-Vanadium Redox Flow Battery, *Electrochim. Acta*, 2007, **52**(24), 6755–6762, DOI: 10.1016/j.electacta.2007.04.121.
32 Z. He, Y. Jiang, Y. Li, *et al.*, Carbon Layer-Exfoliated, Wettability-Enhanced, SO_3H-Functionalized Carbon Paper: A Superior Positive Electrode for Vanadium Redox Flow Battery, *Carbon*, 2018, **127**, 297–304, DOI: 10.1016/j.carbon.2017.11.006.
33 B. Sun and M. Skyllas-Kazacos, Modification of Graphite Electrode Materials for Vanadium Redox Flow Battery Application—I. Thermal Treatment, *Electrochim. Acta*, 1992, **37**(7), 1253–1260, DOI: 10.1016/0013-4686(92)85064-R.
34 K. V. Greco, A. Forner-Cuenca, A. Mularczyk, J. Eller and F. R. Brushett, Elucidating the Nuanced Effects of Thermal Pretreatment on Carbon Paper Electrodes for Vanadium Redox Flow Batteries, *ACS Appl. Mater. Interfaces*, 2018, **10**(51), 44430–44442, DOI: 10.1021/acsami.8b15793.
35 E. Agar, C. R. Dennison, K. W. Knehr and E. C. Kumbur, Identification of Performance Limiting Electrode Using Asymmetric Cell Configuration in Vanadium Redox Flow Batteries, *J. Power Sources*, 2013, **225**, 89–94, DOI: 10.1016/j.jpowsour.2012.10.016.
36 Y. Li, J. Parrondo, S. Sankarasubramanian and V. Ramani, Impact of Surface Carbonyl- and Hydroxyl-Group Concentrations on Electrode Kinetics in an All-Vanadium

Redox Flow Battery, *J. Phys. Chem. C*, 2019, **123**(11), 6370–6378, DOI: 10.1021/acs.jpcc.8b11874.

37 G. Wei, X. Fan, J. Liu and C. Yan, Electrospun Carbon Nanofibers/Electrocatalyst Hybrids as Asymmetric Electrodes for Vanadium Re.dox Flow Battery, *J. Power Sources*, 2015, **281**, 1–6, DOI: 10.1016/j.jpowsour.2015.01.161.

38 M. Jing, A. Zhang, N. Liu, *et al.*, Asymmetric Batteries Based on Customized Positive and Negative Electrodes-an Effective Strategy to Further Improve the Performance of Vanadium Redox Flow Batteries, *Electrochim. Acta*, 2024, **473**, 143478, DOI: 10.1016/j.electacta.2023.143478.

39 M. Y. Lu, W. W. Yang, X. S. Bai, Y. M. Deng and Y. L. He, Performance Improvement of a Vanadium Redox Flow Battery with Asymmetric Electrode Designs, *Electrochim. Acta*, 2019, **319**, 210–226, DOI: 10.1016/j.electacta.2019.06.158.

40 P. Mazúr, J. Mrlík, J. Beneš, *et al.*, Performance Evaluation of Thermally Treated Graphite Felt Electrodes for Vanadium Redox Flow Battery and Their Four-Point Single Cell Characterization, *J. Power Sources*, 2018, **380**, 105–114, DOI: 10.1016/j.jpowsour.2018.01.079.

41 J. Xu, Y. Zhang, Z. Huang, C. Jia and S. Wang, Surface Modification of Carbon-Based Electrodes for Vanadium Redox Flow Batteries, *Energy Fuels*, 2021, **35**(10), 8617–8633, DOI: 10.1021/acs.energyfuels.1c00722.

42 G. Nikiforidis, Y. Xiang and W. A. Daoud, Electrochemical Behavior of Carbon Paper on Cerium Methanesulfonate Electrolytes for Zinc-Cerium Flow Battery, *Electrochim. Acta*, 2015, **157**, 274–281, DOI: 10.1016/j.electacta.2014.11.134.

43 A. Kaur, K. I. Jeong, S. S. Kim and J. W. Lim, Optimization of Thermal Treatment of Carbon Felt Electrode Based on the Mechanical Properties for High-Efficiency Vanadium Redox Flow Batteries, *Compos. Struct.*, 2022, **290**, 115546, DOI: 10.1016/j.compstruct.2022.115546.

44 H. Lim, M. Shin, C. Noh, E. Koo, Y. Kwon and K. Y. Chung, Performance Evaluation of Aqueous All Iron Redox Flow Batteries Using Heat Treated Graphite Felt Electrode, *Korean J. Chem. Eng.*, 2022, **39**(11), 3146–3154, DOI: 10.1007/s11814-022-1195-z.

45 G. Nikiforidis and W. A. Daoud, Thermally Modified Graphite Electrodes for the Positive Side of the Zinc-Cerium Redox Flow Battery, *J. Electrochem. Soc.*, 2015, **162**(6), A809–A819, DOI: 10.1149/2.0041506jes.

46 L. Faggiano, G. Lacarbonara, W. D. Badenhorst, L. Murtomäki, L. Sanz and C. Arbizzani, Short Thermal Treatment of Carbon Felts for Copper-Based Redox Flow Batteries, *J. Power Sources*, 2022, **520**, 230846, DOI: 10.1016/j.jpowsour.2021.230846.

47 A. J. Bard and L. R. Faulkner, *Electrochemical Methods: Fundamentals and Applications*, Wiley, New York Weinheim, 2nd edn, 2000.

48 H. Dong, J. Chen, L. Feng, W. Zhang, X. Guan and T. J. Strathmann, Degradation of Organic Contaminants through Activating Bisulfite by Cerium(IV): A Sulfate Radical-Predominant Oxidation Process, *Chem. Eng. J.*, 2019, **357**, 328–336, DOI: 10.1016/j.cej.2018.09.024.

49 R. S. Nicholson and I. Shain, Theory of Stationary Electrode Polarography. Single Scan and Cyclic Methods Applied to Reversible, Irreversible, and Kinetic Systems, *Anal. Chem.*, 1964, **36**(4), 706–723, DOI: 10.1021/ac60210a007.

50 R. S. Nicholson, Theory and Application of Cyclic Voltammetry for Measurement of Electrode Reaction Kinetics, *Anal. Chem.*, 1965, **37**(11), 1351–1355, DOI: 10.1021/ac60230a016.

51 R. J. Klingler and J. K. Kochi, Electron-Transfer Kinetics from Cyclic Voltammetry. Quantitative Description of Electrochemical Reversibility, *J. Phys. Chem.*, 1981, **85**(12), 1731–1741, DOI: 10.1021/j150612a028.

52 T. Herr, P. Fischer, J. Tübke, K. Pinkwart and P. Elsner, Increasing the Energy Density of the Non-Aqueous Vanadium Redox Flow Battery with the Acetonitrile-1,3-Dioxolane–Dimethyl Sulfoxide Solvent Mixture, *J. Power Sources*, 2014, **265**, 317–324, DOI: 10.1016/j.jpowsour.2014.04.141.

53 I. Gunasekara, M. N. Ates, S. Mukerjee, E. J. Plichta, M. A. Hendrickson and K. M. Abraham, Solid Phase FePC Catalysts for Increased Stability of Oxygen Reduction Reaction Intermediates at the Cathode/Electrolyte Interface in Lithium Air Batteries, *J. Electrochem. Soc.*, 2017, **164**(4), A760–A769, DOI: 10.1149/2.1221704jes.

54 Z. Masood, H. Muhammad and I. A. Tahiri, Comparison of Different Electrochemical Methodologies for Electrode Reactions: A Case Study of Paracetamol, *Electrochem*, 2024, **5**(1), 57–69, DOI: 10.3390/electrochem5010004.

55 J. H. Savéant and D. Tessier, Variation of the Electrochemical Transfer Coefficient with Potential, *Faraday Discuss. Chem. Soc.*, 1982, **74**, 57–72, DOI: 10.1039/DC9827400057.

56 E. J. F. Dickinson and A. J. Wain, The Butler-Volmer Equation in Electrochemical Theory: Origins, Value, and Practical Application, *J. Electroanal. Chem.*, 2020, **872**, 114145, DOI: 10.1016/j.jelechem.2020.114145.

57 J. M. Nzikou, M. Aurousseau and F. Lapicque, Electrochemical Investigations of the Ce(III)/Ce(IV) Couple Related to a Ce(IV)-Assisted Process for SO_2/NO_x Abatement, *J. Appl. Electrochem.*, 1995, **25**, 967–972, DOI: 10.1007/BF00241592.

58 Z. Xie, D. Zhou, F. Xiong, S. Zhang and K. Huang, Cerium-Zinc Redox Flow Battery: Positive Half-Cell Electrolyte Studies, *J. Rare Earths*, 2011, **29**(6), 567–573, DOI: 10.1016/S1002-0721(10)60499-1.

59 Y. Gao, H. Wang, Q. Ma, *et al.*, Carbon Sheet-Decorated Graphite Felt Electrode with High Catalytic Activity for Vanadium Redox Flow Batteries, *Carbon*, 2019, **148**, 9–15, DOI: 10.1016/j.carbon.2019.03.035.

60 D. O. Opar, R. Nankya, J. Lee and H. Jung, Assessment of Three-Dimensional Nitrogen-Doped Mesoporous Graphene Functionalized Carbon Felt Electrodes for High-Performance All Vanadium Redox Flow Batteries, *Appl. Surf. Sci.*, 2020, **531**, 147391, DOI: 10.1016/j.apsusc.2020.147391.

61 Y. A. Gandomi, D. S. Aaron, J. R. Houser, *et al.*, Critical Review—Experimental Diagnostics and Material Characterization Techniques Used on Redox Flow

Batteries, *J. Electrochem. Soc.*, 2018, **165**(5), A970–A1010, DOI: 10.1149/2.0601805jes.

62 T. C. Chang, J. P. Zhang and Y. K. Fuh, Electrical, Mechanical and Morphological Properties of Compressed Carbon Felt Electrodes in Vanadium Redox Flow Battery, *J. Power Sources*, 2014, **245**, 66–75, DOI: 10.1016/j.jpowsour.2013.06.018.

63 P. Bai and M. Z. Bazant, Performance and Degradation of A Lithium-Bromine Rechargeable Fuel Cell Using Highly Concentrated Catholytes, *Electrochim. Acta*, 2016, **202**, 216–223, DOI: 10.1016/j.electacta.2016.04.010.

64 P. C. Ghimire, A. Bhattarai, R. Schweiss, G. G. Scherer, N. Wai and Q. Yan, A Comprehensive Study of Electrode Compression Effects in All Vanadium Redox Flow Batteries Including Locally Resolved Measurements, *Appl. Energy*, 2018, **230**, 974–982, DOI: 10.1016/j.apenergy.2018.09.049.

65 J. Charvát, P. Mazúr, J. Dundálek, *et al.*, Performance Enhancement of Vanadium Redox Flow Battery by Optimized Electrode Compression and Operational Conditions, *J. Energy Storage*, 2020, **30**, 101468, DOI: 10.1016/j.est.2020.101468.

66 R. Gundlapalli and S. Jayanti, Effect of Electrode Compression and Operating Parameters on the Performance of Large Vanadium Redox Flow Battery Cells, *J. Power Sources*, 2019, **427**, 231–242, DOI: 10.1016/j.jpowsour.2019.04.059.

67 P. K. Leung, C. Ponce-de-León, C. T. J. Low, A. A. Shah and F. C. Walsh, Characterization of a Zinc–Cerium Flow Battery, *J. Power Sources*, 2011, **196**(11), 5174–5185, DOI: 10.1016/j.jpowsour.2011.01.095.

68 Y. Li, P. Geysens, X. Zhang, *et al.*, Cerium-Containing Complexes for Low-Cost, Non-Aqueous Redox Flow Batteries (RFBs), *J. Power Sources*, 2020, **450**, 227634, DOI: 10.1016/j.jpowsour.2019.227634.

69 J. Wu, X. Cao, Y. Ji, *et al.*, Boosting Kinetics of Ce^{3+}/Ce^{4+} Redox Reaction by Constructing TiC/TiO2 Heterojunction for Cerium-Based Flow Batteries, *Adv. Funct. Mater.*, 2024, **34**(3), 2309825, DOI: 10.1002/adfm.202309825.

70 S. Yun, J. Parrondo and V. Ramani, Derivatized Cardo-Polyetherketone Anion Exchange Membranes for All-Vanadium Redox Flow Batteries, *J. Mater. Chem. A*, 2014, **2**(18), 6605–6615, DOI: 10.1039/C4TA00166D.

71 S. Yun, J. Parrondo and V. Ramani, Composite Anion Exchange Membranes Based on Quaternized Cardo-Poly(Etherketone) and Quaternized Inorganic Fillers for Vanadium Redox Flow Battery Applications, *Int. J. Hydrogen Energy*, 2016, **41**(25), 10766–10775, DOI: 10.1016/j.ijhydene.2016.04.060.

72 S. I. U. Ahmed and S. Sankarasubramanian, Low pH Titanium Electrochemistry in the Presence of Sulfuric Acid and Its Implications for Redox Flow Battery Applications, *J. Electrochem. Soc.*, 2024, **171**(6), 60538, DOI: 10.1149/1945-7111/ad5975.

73 J. Seo, S. Sankarasubramanian, N. Singh, F. Mizuno, K. Takechi and J. Prakash., Effect of Cathode Porosity on the Lithium-Air Cell Oxygen Reduction Reaction – A Rotating Ring-Disk Electrode Investigation, *Electrochim. Acta*, 2017, **248**, 570–577, DOI: 10.1016/j.electacta.2017.07.121.

74 E. Asadipour and V. K. Ramani, A Computationally-cost Effective Model for Fluid Flow in Redox Flow Batteries, *AIChE J.*, 2023, **69**(7), e18051, DOI: 10.1002/aic.18051.

